Journal of the European Ceramic Society 46 (2026) 118150

Contents lists available at ScienceDirect

Journal of the European Ceramic Society

journal homepage: www.elsevier.com/locate/jeurceramsoc

Scalable single-step fabrication of high-entropy oxide coatings by axial solution precursor plasma spray

Gidla Vinay [a,*], Stefan Björklund [b], Ilari Angervo [c], Ashish Ganvir [a], Shrikant Joshi [b]

[a] Department of Mechanical and Materials Engineering, University of Turku, Finland
[b] Department of Engineering Science, University West, Sweden
[c] Department of Physics and Astronomy, University of Turku, Finland

ARTICLE INFO

Keywords:
High entropy oxide
Solution precursor plasma spray
Thermal spray
Single-step
Battery electrode

ABSTRACT

High-entropy oxides (HEOs) are promising for energy and structural applications, yet conventional synthesis routes yield powders that require multiple post-processing steps before use. This study demonstrates single-step fabrication of a transition-metal HEO coating via axial-fed solution precursor plasma spraying (SPPS) using equimolar Co-Cu-Mg-Ni-Zn nitrate hydrates. The resulting coatings are dense, adherent, and phase-pure, exhibiting a rock-salt structure confirmed by XRD, uniform cation distribution by SEM/EDS, and oxidized cations with oxygen-vacancy signatures by XPS. Comparative analysis of different spray conditions shows that phase purity and microstructure are governed by atomization and in-flight residence time, rather than plasma energy alone. The findings establish that suitable parameter control enables complete cation mixing and rapid in-flight phase formation without post-processing. This single-step route from solution to functional coatings provides a scalable pathway for HEO manufacture, with potential applications ranging from battery electrodes to high-temperature thermal and environmental barrier coatings (TBCs/EBCs) across different HEO families.

1. Introduction

The concept of high-entropy materials, originally developed for metallic alloys, was extended to oxide systems by Rost et al. [1] in 2015, leading to the emergence of high-entropy oxides (HEOs) [1–3]. Analogous to high-entropy alloys (HEAs), HEOs typically contain five or more metal cations in near-equimolar ratios, forming a single-phase crystal structure stabilized by high configurational entropy. The inherent thermodynamic and structural stability of oxides at elevated temperatures makes HEOs attractive for high-temperature applications such as thermal barrier coatings (TBCs) and environmental barrier coatings (EBCs) [4,5]. In addition, their rich defect chemistry including high oxygen vacancy concentrations and multivalent redox behavior offers potential in functional applications such as lithium-ion batteries (LIBs), all-solid-state batteries (ASSBs), and electrocatalysis [6,7]. HEOs can be classified by cation type (transition-metal (TM), rare-earth (RE), or mixed TM-RE systems) or by crystal structure, such as rock-salt, spinel, perovskite, fluorite, pyrochlore, and rutile [3]. A wide variety of synthesis routes have been explored for producing HEOs, including mechanical alloying [1], co-precipitation [8], hydrothermal processing [9], sol-gel routes [10], and solution-combustion methods [11], along with broader methodological reviews that summarize their advantages and limitations [12,13]. While these wet-chemical approaches enable good compositional control, they remain multi-step processes requiring calcination, grinding, and powder conditioning, and are therefore not readily scalable for coating fabrication or for electrode architectures in emerging energy devices. Specifically for LIB/ASSB electrodes as an example, this entails additional slurry preparation, casting, drying, and sintering, while for TBC/EBC coatings, powders within a defined particle size range must subsequently be thermal-sprayed. In both cases, strict particle size requirements further limit the yield of a synthesis route that is already time-consuming and costly. These challenges highlight the need for alternative, application-dependent direct HEO fabrication methods wherever relevant.

To address this need, plasma spraying has emerged as a promising route for scalable, high-throughput manufacturing of functional oxides. Beyond its established use in protective coatings, recent work has demonstrated its potential for directly fabricating battery electrodes [14–17]. While TM-HEOs such as (Co-Cu-Mg-Ni-Zn)O have shown promise as battery electrodes, prior studies have relied on pre-synthesized powders and conventional electrode fabrication [18]. Recent work has demonstrated the feasibility of producing HEO powders

* Corresponding author.
E-mail address: vinay.gidla@utu.fi (G. Vinay).

https://doi.org/10.1016/j.jeurceramsoc.2026.118150
Received 5 November 2025; Received in revised form 12 January 2026; Accepted 15 January 2026
Available online 16 January 2026

by SPPS [19]. Amarnath et al. [20] reported HEO coatings in a Ni-Fe-Mn-Cu-Co system for water splitting, while Lin et al. [21] demonstrated coatings in a Fe-Co-Ni-Cu-Zn-Mg system. These studies highlight the feasibility of HEO coating fabrication by SPPS but provide limited insights into processing windows. In earlier work, precursors were injected into legacy radial-feed plasma torches, which are generally associated with lower deposition efficiencies and limited coating throughput [22]. Here, we demonstrate for the first time the in-flight synthesis and direct deposition of (Co-Cu-Mg-Ni-Zn) HEO coatings via SPPS, emphasizing the role of process parameters. The choice of (Co-Cu-Mg-Ni-Zn) HEO was motivated by it being one of the most widely studied HEO systems and by its promise as an anode material for LIBs and ASSBs. This is also the first report of using axial feeding (Fig. 1) of precursor solution rather than radial injection. Axial feeding provides more effective utilization of thermal energy in the plasma torch and a more uniform energy distribution to the droplets, enabling higher output. In SPPS, the precursor droplet undergoes atomization, solvent/hydrate evaporation, decomposition to oxides (pyrolysis), and melting/semi-melting before deposition (Fig. 1). This sequence becomes more complex in multi-constituent systems such as HEOs, making appropriate process parameter control essential to achieve single-phase coatings during the short in-flight residence time. This study demonstrates that such control is indeed possible. By varying process parameters that influence enthalpy input, we establish a framework showing that SPPS is amenable to controlled, rapid one-step conversion of precursor solutions into functional coatings. In this context, SPPS can be regarded as a plasma-assisted spray pyrolysis process, but unlike conventional flame spray pyrolysis (FSP) and nebulized spray pyrolysis (NSP) routes, it directly yields coatings rather than powders, thereby bypassing multiple post-processing steps. This approach not only demonstrates easily scalable pathways for HEO-based energy storage electrodes but also provides guidelines for extending SPPS to other HEO families for diverse applications.

2. Materials and methodology

Analytical-grade metal nitrate hydrates $Co(NO_3)_2{\cdot}6\ H_2O$ (291.03 $g{\cdot}mol^{-1}$), $Cu(NO_3)_2{\cdot}2.5\ H_2O$ (232.59 $g{\cdot}mol^{-1}$), $Mg(NO_3)_2{\cdot}6\ H_2O$ (256.40 $g{\cdot}mol^{-1}$), $Ni(NO_3)_2{\cdot}6\ H_2O$ (290.80 $g{\cdot}mol^{-1}$), and $Zn(NO_3)_2{\cdot}6\ H_2O$ (297.48 $g{\cdot}mol^{-1}$) obtained from Sigma Aldrich were used. The salts were dissolved in distilled water and then mixed in equimolar proportions to a prepare a 1.0 M total cation solution. The solution was stirred until homogeneous to ensure stable feeding to the plasma torch. Coatings were deposited using a Mettech Axial III high-power plasma torch (Northwest Mettech Corp., Vancouver, Canada) equipped with a Nanofeed 350 feeding system. The spray parameters for each sample are summarized in Table 1. Disks of aluminum (25 mm diameter, 2 mm thickness) served as substrates and were grit-blasted prior to deposition for improved adhesion. The choice of Al substrate is due to its widespread use as a current collector in lithium-ion battery systems, which represents one of the targeted application areas for the present HEO coatings. Phase analysis was performed on a Panalytical Empyrean diffractometer using Cu Kα radiation (λ = 1.5406 Å). Scans were collected over the 2θ range 20–100° with a step size of 0.02° and 0.008 s per step. Phases were identified using X'Pert HighScore software. Surface and cross-sectional microstructures were examined with a ThermoFisher Apreo FE-SEM equipped with energy-dispersive X-ray spectroscopy (EDS), which was also used to acquire elemental maps. X-ray photoelectron spectroscopy (XPS) was carried out using a ThermoFisher Nexsa (ESCA) system. Survey scans employed a step size of 1 eV across the 0–1350 eV range, while core-level scans used a step size of 0.1 eV. Data were processed using Avantage software, with charge correction performed using the C-C peak in C1s as the reference. Samples were Ar^+ etched prior to XPS data acquisition.

3. Results

The surface morphologies of the three coatings (S1, S2, S3) are shown in Fig. 2a-c, with corresponding higher-magnification images in Fig. 2d-f. Coatings S2 (Fig. 2b) and S3 (Fig. 2c) display broadly similar morphologies, whereas S1 (Fig. 2a) exhibits a distinctly rougher surface. In S2, numerous micro-cracks are visible on the surface, while these features are markedly reduced in S3. At higher magnification, S2 (Fig. 2e) reveals distinct micro-cracks along surface features, whereas S3 (Fig. 2f) shows more consolidated well-bonded regions with minimal separation. These cracks are most likely associated with thermal contraction during rapid solidification, leading to local separation within the deposit. Elemental distribution maps from EDS analyses (Fig. 2g-i) show detectable aluminum on the S1 surface, indicating incomplete coating coverage and substrate exposure. In contrast, S2 and S3 contain only the intended transition-metal cations (Cu, Mg, Ni, Co, Zn), which are uniformly distributed without detectable aluminum.

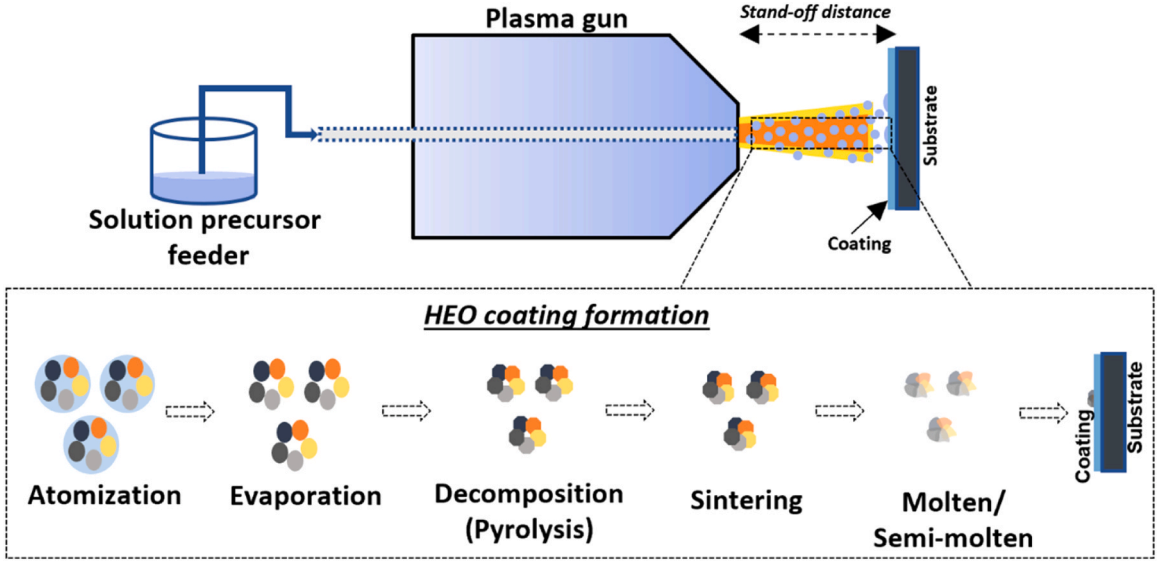

Fig. 1. Schematic of the axial-injection SPPS process. The precursor solution is injected along the torch axis into the plasma plume, where droplets undergo atomization, solvent and hydrate evaporation, thermal decomposition of nitrates to oxides (pyrolysis), melting/semi-melting, and finally impact and solidification to form a high-entropy oxide coating.

Table 1
SPPS process parameters used for coating generation.

Sample	Nozzle dia (Inches)	Current (A)	Power (kW)	Gas flow ($l \cdot min^{-1}$)	Gas mixture composition ($Ar/N_2/H_2$)	Enthalpy ($kJ \cdot g^{-1}$)
S1 coating	5/16	200	130	300	44/28/28	12.5
S2 coating	5/16	180	88	300	80/10/10	6.9
S3 coating	5/16	200	107	200	70/20/10	9.0

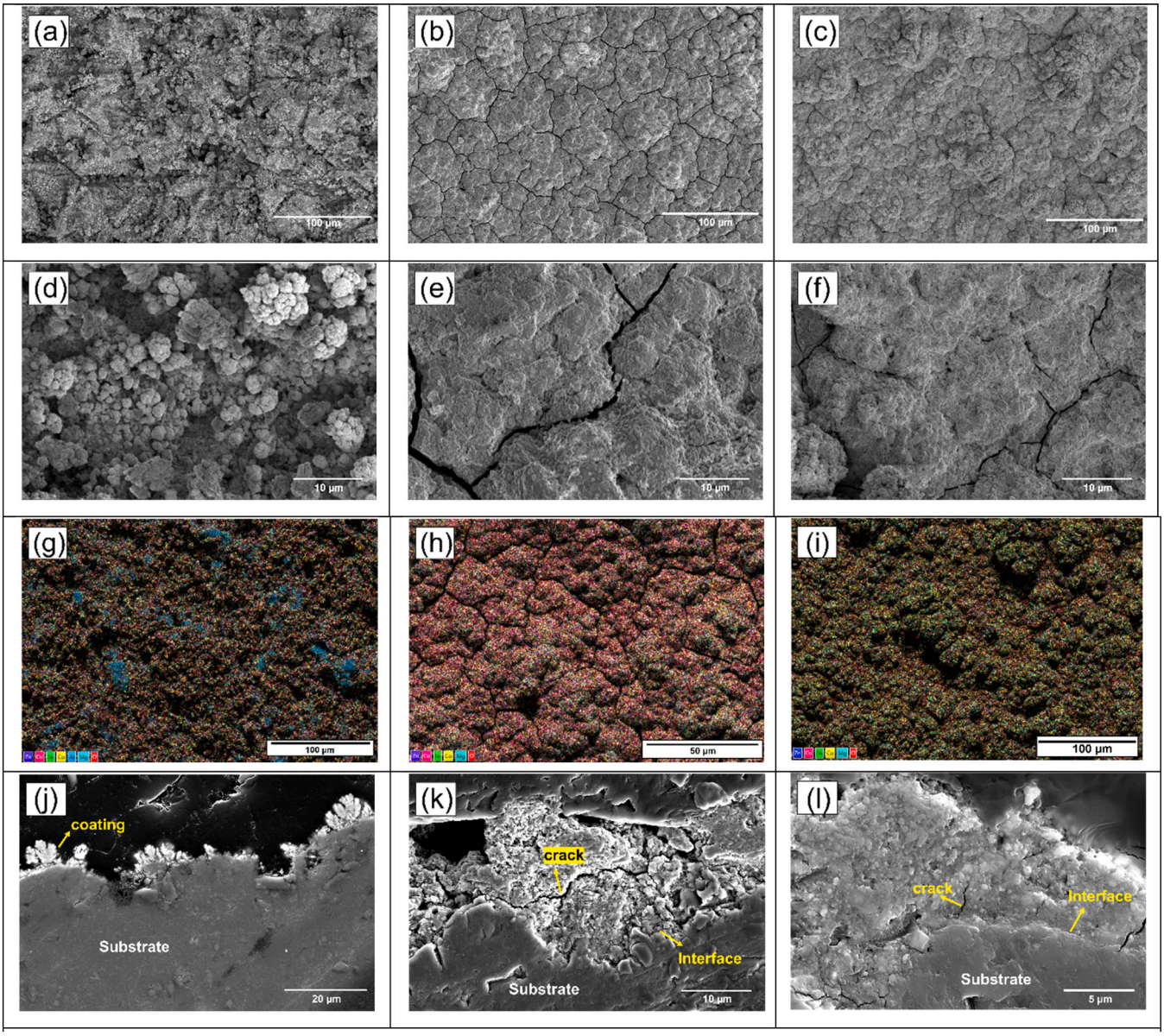

Fig. 2. SEM surface images of the three generated coatings: (a) S1 Coating, (b) S2 coating, (c) S3 coating, and their respective high-magnification images highlighting: (d) flower-like protrusions in S1 coating, (e) micro-cracks in S2 coating, (f) well-bonded regions in S3 coating; Surface EDS overlay image of all elements present in: (g) S1 coating, (h) S2 coating, (i) S3 coating; Cross section SEM images of the coatings highlighting: (j) flower-like structure with discontinuous coating in S1, (k) thick coating with cracks and poor adhesion in S2, (l) dense coating with minimal cracks and good substrate adhesion in S3.

Cross-sectional SEM images (Fig. 2j-l) further differentiate the coatings. The S1 (Fig. 2j) exhibits a "flower-like" and feathery morphology typical of poorly adhered deposits, with isolated flakes and minimal substrate coverage. In comparison, S2 (Fig. 2k) and S3 (Fig. 2l) form continuous coatings. S2 exhibits greater thickness but contains a network of vertical and lateral cracks, consistent with the surface morphology observations, whereas S3 forms a relatively denser, well-adhered layer.

The XRD patterns of the three coatings are shown in Fig. 3, with the raw data presented in Supplementary Fig. S1a-c. In the raw patterns, peaks from the aluminum substrate are visible due to the limited coating thickness observed in Fig. 2, resulting in partial X-ray penetration into the substrate. The patterns in Fig. 3 were processed to remove the substrate contributions, allowing clearer identification of the coating phases. For the S3 sample, the diffraction peaks at $2\theta \sim 36°$, 43°, 63°, and

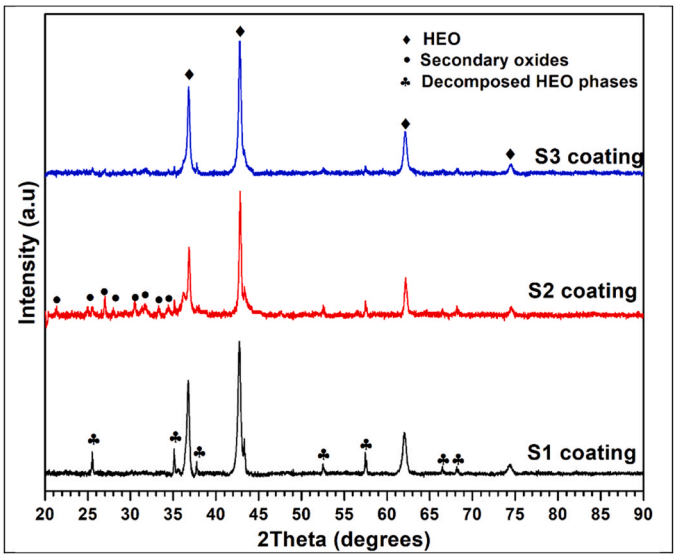

Fig. 3. XRD comparison of S1, S2 and S3 coatings highlighting the different phases present. Substrate (Al) contributions visible in raw data were removed for clarity (see Fig. S1).

74° correspond to a single-phase rock-salt structure, consistent with literature reports for (Co-Cu-Mg-Ni-Zn)O based HEOs [1,23]. The expected peak at ~80° coincides with a strong aluminum substrate reflection and was therefore removed during filtering. The S2 coating, which exhibits the greatest thickness, also shows dominant rock-salt reflections but with additional minor peaks attributable to secondary oxide phases [1,24]. These weak secondary reflections are assigned to non-rock-salt oxides that are not yet fully incorporated into the high-entropy solid solution during deposition, indicating incomplete in-flight homogenization. In contrast, S1 shows rock-salt peaks accompanied by a few sharp secondary peaks. We attribute these to low-temperature re-segregation from a formed rock-salt HEO during rapid cooling and/or insufficient residence near the stabilizing temperature, consistent with prior reports that rock-salt (Co-Cu-Mg-Ni-Zn)O reversibly develops tenorite and spinel peaks when equilibrated below ~850–900 °C and returns to single-phase rock-salt on reheating [1,25,26]. Overall, these results show that S3 achieves a phase-pure rock-salt HEO structure, S2 contains a predominantly rock-salt phase with residual secondary oxides (precursor-derived oxides persisting), and S1 exhibits post-formation re-segregation from the HEO during/after impact.

High-magnification SEM imaging of the S3 surface (Fig. 4a) reveals fine, nanometer-scale crystalline grains. Corresponding elemental distribution maps (Fig. 4b-h) confirm that all major constituent elements (Cu, Mg, Ni, Co, Zn) are uniformly distributed across both the surface and within individual grains. Quantitative EDS analysis from multiple areas (Table 2) shows that Mg is present at a slightly higher atomic percentage compared with the other cations, while the remaining elements are close to equimolar ratios. This enrichment may be due to the high melting point and lower volatility of MgO relative to the other oxides, which requires further analysis. Cross-sectional EDS mapping of the S3 coating (Supplementary Fig. S2 and S3) further confirms uniform

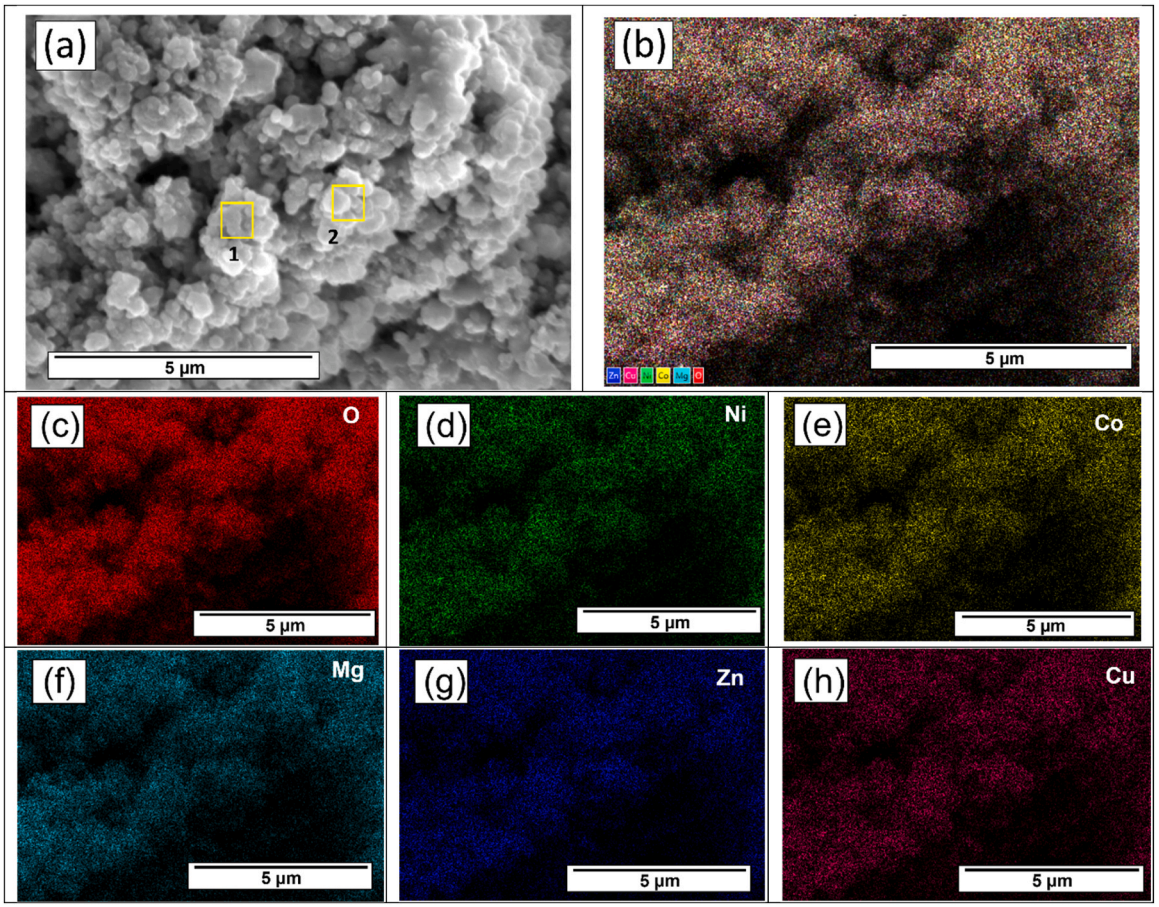

Fig. 4. Surface microstructure and chemistry of S3: (a) SEM shows fine, nanocrystalline grains, (b) EDS overlay confirms the presence and uniform distribution of Cu, Mg, Ni, Co, Zn, and O, (c-h) Element specific EDS maps (O, Ni, Co, Mg, Zn, Cu) demonstrate uniformity at the grain scale. Quantitative EDS at two surface sites is reported in Table 2.

Table2
EDS atomic percentages at two surface sites of S3 (locations marked in Fig. 4a). Cation ratios are close to equimolar with slight Mg enrichment.

Element	Site1 (at%)	Site2 (at%)
O	46.7	44.7
Mg	14.9	13.2
Ni	8.8	9.5
Co	9.9	10.8
Cu	9.8	10.8
Zn	9.9	11

elemental distribution through the coating thickness and good interfacial integrity with the substrate. While the deviation from the ideal equimolar composition may slightly reduce the configurational entropy from the theoretical value of 1.609 R, literature reports indicate that single-phase rock-salt HEO structures can still form under such conditions [27]. This compositional variation could also explain the observed change in relative XRD peak intensities (Fig. 3). In the ideal equimolar case the (111) reflection at ~36° is the most intense, whereas in S3, the intensities of the ~36° and ~43° peaks are altered, consistent with previous studies on non-equimolar variants of (Co-Cu-Mg-Ni-Zn)O systems [27].

XPS was used to determine the oxidation states of the constituent elements in the coatings. The survey spectrum of S3 (Fig. 5a) shows all major elements (Cu, Mg, Ni, Co, Zn, O) without any residual salt-related signals, confirming complete decomposition of the nitrate precursors during plasma spraying. The carbon spectrum is shown in Fig. 5b after the charge correction to C-C reference at 284.8 eV. The C1s shows predominantly three peaks at 284.87 eV, 287.13 eV and 288.72 eV correspond to C-C, C-O and C═O respectively. The Ni 2p spectrum (Fig. 5c) displays peaks corresponding to Ni^{2+} and Ni^{3+} at binding energies of 854.66 eV and 856.64 eV, respectively, along with shake-up satellite peaks at 861.08 eV and 865.02 eV, indicating the presence of nickel oxides. Similar results were obtained for the other cations: Co 2p (Fig. 5d) shows Co^{2+} and Co^{3+} states at 779.79 eV and 782.06 eV, Zn is present as ZnO as observed at 1020.5 eV (Fig. 5e), and Cu exhibits Cu^{2+} and Cu^{1+} peaks at 932.42 eV and 934.09 eV respectively along with characteristic shake-up satellites at 940.42 and 942.98 eV (Fig. 5f). The Cu LMM Auger feature in (Fig. S4a) further confirms this oxidized state. The Mg 1 s peak appears at 1303.16 eV (Fig. 5g), which usually

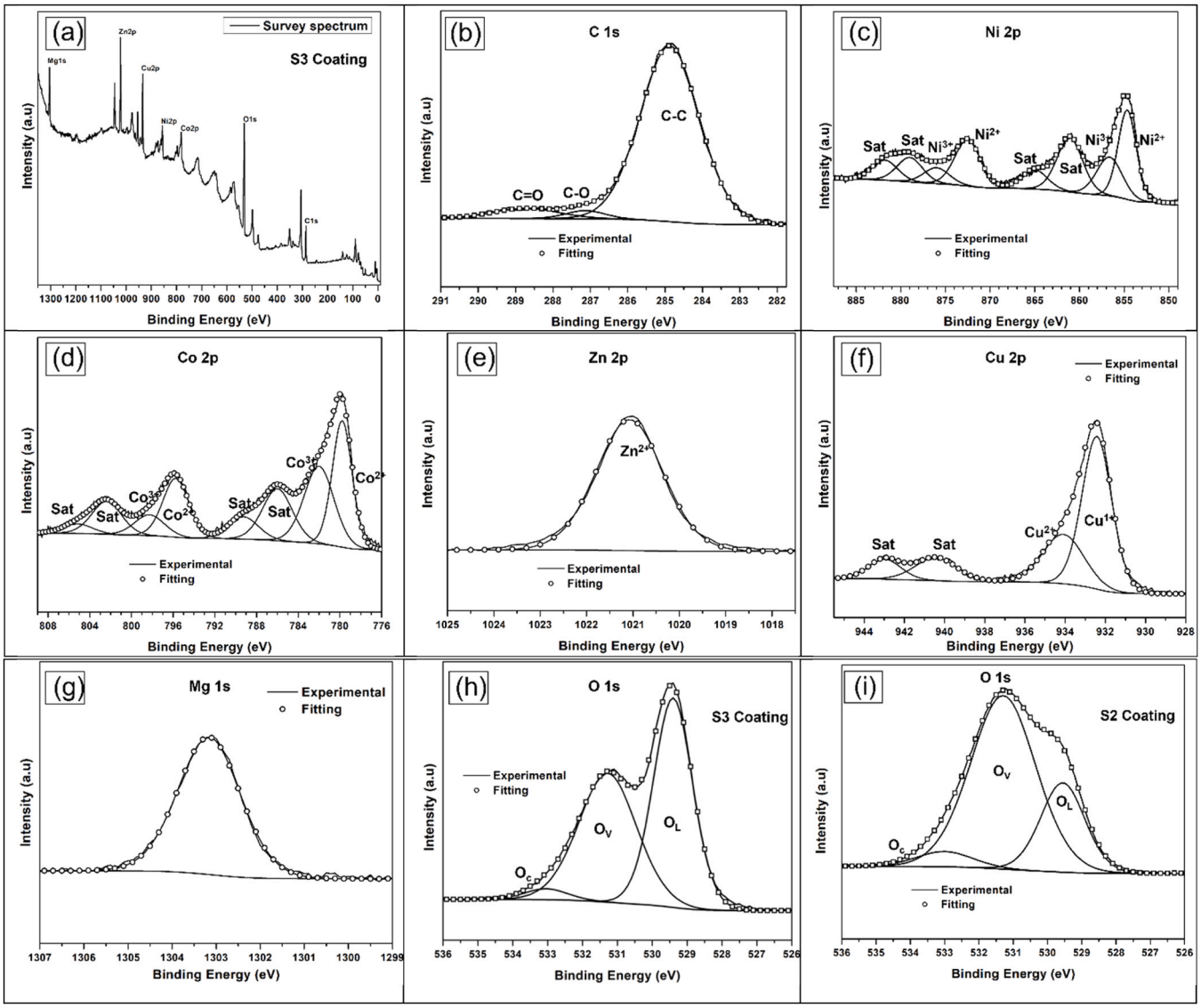

Fig. 5. XPS spectra of the S3 coating: (a) Survey spectrum highlighting no residual nitrate signals, Individual element core level spectrum highlighting different chemical states present in (b) C 1 s (charge reference at 284.8 eV), (c) Ni 2p, (d) Co 2p, (e) Zn 2p, (f) Cu 2p, (g) Mg 1 s, (h) O1s; (i) O 1 s in S2 coating highlighting the increase in O_V compared with S3 coating.

corresponds to metallic Mg. Given Mg's high reactivity with oxygen at elevated temperatures, the formation of metallic Mg during deposition is highly unlikely. The observed signal is more plausibly due to partial reduction during the Ar^+ ion etching step performed prior to data collection. The shift in the Mg peak during with the Ar^+ ion beam etching obtained from the survey spectrum is shown in the Fig. S4b further confirms this claim. The O 1 s spectrum for S3 (Fig. 5h) shows a main peak at 529.7 eV associated with metal oxygen bonds and a secondary peak at 531.28 eV corresponding to oxygen vacancy defects [27]. These defect sites are known to play a significant role in electrochemical energy storage [28]. Comparison with the O 1 s spectrum of S2 (Fig. 5i) reveals a higher relative intensity of the defect-related peak in S2. This is likely due to the increased grain boundary area associated with secondary phases, as observed in XRD, which can act as preferential sites for oxygen vacancy formation [29,30]. Alternatively, it could also be related to hydroxyl adsorption on secondary oxides or complex phases, which are often misinterpreted as oxygen vacancies [31]. It would be interesting to investigate how these defects affect electrochemical performance, particularly if they indeed originate from oxygen vacancies at grain boundaries, which requires further study.

4. Discussion

The phase stability of high-entropy oxides (HEOs) is governed by the Gibbs free energy relation:

$$\Delta G = \Delta H - T\Delta S \quad (1)$$

where ΔH represents the enthalpy cost of bond breaking and reformation into a single-phase lattice, and $T\Delta S$ is the stabilizing energy from configurational entropy. For the (Co-Cu-Mg-Ni-Zn)O system, the configurational entropy is reported as $\Delta S_{Config.} \sim 1.609$ R, Rost et al. [1] suggested $\Delta H_{mix} = \sim +10\ \mathrm{kJ{\cdot}mol^{-1}}$ of cation sites, with an entropy stabilization temperature of $T_C > 875°C$. It is proposed that above these temperatures the entropy dominates the enthalpy mix and results in stabilization of the system in rock-salt solid solution [1,23]. Process temperatures in plasma spray typically exceed this range [32], melting the material and followed by rapid solidification, thereby defining the practical processing window. Since the feedstock is supplied in the form of precursor mix of all cations, the overall energy in the plasma spray should be enough to decompose all the cation precursors then achieve the enthalpy mix, melt the material and then deposit on the substrate followed by rapid solidification, which kinetically locks the structure. In this regard the total enthalpy requirement for this to happen could be expressed as below.

$$\Delta H_{req.} = \Delta H_{decomp.} + \Delta H_{crystal\ water.} + \Delta H_{solvent\ evap.} + \Delta H_{mix} \quad (2)$$

In Eq.2., $\Delta H_{decomp.}$, corresponds to the energy required to decompose the metal nitrates into their respective oxides in-flight, $\Delta H_{crystal\ water.}$ represents the enthalpy for the removal of crystal-bound water in the hydrates, while $\Delta H_{solvent\ evap.}$ accounts for the evaporation of additional solvent water used for precursor dissolution. Finally, ΔH_{mix} denoted the enthalpy associated with cation mixing to form single-phase HEO lattice. It is well reported that processes such as nebulized spray pyrolysis (NSP) [33] and flame spray pyrolysis (FSP) [23] can exceed T_C during droplet flight, enabling in-flight rock-salt phase formation that is then kinetically locked by rapid quenching. SPPS also falls into this category and can achieve even higher in-flight temperatures; however, the effective energy available to each droplet depends on plasma precursor interaction efficiency, droplet trajectory, and plume energy losses.

$$\Delta H_{decomp} = \Sigma\Delta H^{\circ}f_{(oxides)} - \Sigma\Delta H^{\circ}f_{(nitrates)} \quad (3)$$

The decomposition enthalpies for each nitrate are well documented, and using Hess's law the decomposition enthalpy for each oxide can be calculated [34]. For an equimolar Co/Ni/Mg/Zn/Cu nitrate feed, the nitrate-to-oxide decomposition at 298 K sums to 1159.01 kJ for one mole of each salt, corresponding to 1.301 $\mathrm{kJ{\cdot}g^{-1}}$ on an anhydrous basis (total anhydrous mass = 890.876 g). On the hydrate basis actually fed (total mass = 1368.3 g as described in the methodology), the same decomposition term is 0.847 $\mathrm{kJ{\cdot}g^{-1}}$. Removal of crystal-bound water (25–100 °C including vaporization) adds ~0.899 $\mathrm{kJ{\cdot}g^{-1}}$ [35], while a modest cation mixing enthalpy of ~10 $\mathrm{kJ{\cdot}mol^{-1}}$ per cation contributes ~0.04 $\mathrm{kJ{\cdot}g^{-1}}$. In addition, the evaporation of extra solvent water used for precursor dissolution contributes ~2.57 $\mathrm{kJ{\cdot}g^{-1}}$ per gram of water. On a per-solution basis, considering the hydrate-to-solvent mass fractions (0.493:0.507), the total enthalpy requirement is ~2.18 $\mathrm{kJ{\cdot}g^{-1}}$ (detailed calculation provided in the Supplementary File). These values are much smaller than the measured SPPS process enthalpies which are 12.5, 6.9, and 9 $\mathrm{kJ{\cdot}g^{-1}}$ for the S1, S2, and S3 coatings respectively as reported in Table1. These measured enthalpies already include system losses. This confirms that the plasma provides more than enough thermal energy to drive the required chemistry even for a five-cation mixture. However, as observed in Fig. 3, the presence of secondary phases in S1 and S2 shows that energy availability alone does not guarantee single-phase retention. The decisive factors are how effectively this energy is coupled to the droplets, their residence time in the hot zone, and their trajectories within the plasma plume. Thus, exceeding $\Delta H_{req.}$ is necessary but not sufficient to ensure complete single-phase formation.

In SPPS, a salt solution is injected into the plasma, where droplets undergo atomization, rapid solvent/hydrate evaporation, in-flight decomposition to oxides, and melting/semi-melting before impacting the substrate to form the coating [20,36]. Because solvent evaporation is endothermic, liquid-fed spraying often requires higher torch power than powder APS. Axial injection offers an additional advantage by providing more uniform energy distribution to the droplets and higher effective energy transfer compared with radial injection [22,36]. Consequently, process parameters that regulate energy transfer and residence time such as gas flow, torch power, stand-off distance, injection geometry, and precursor feed/concentration become critical. Our S1, S2, and S3 results illustrate this interplay. S1, processed at the highest enthalpy, did not yield a continuous coating. The excessive plume energy combined with high total gas flow decreases residence time, causing droplet stripping/overspray, and hindered consolidation. XRD confirmed rock-salt reflections accompanied by secondary decomposition products, consistent with formation followed by decomposition under a harsher thermal history [1,25,26]. In contrast, S2, processed at the lowest enthalpy, produced a thick coating but retained secondary phases, indicating incomplete in-flight reactions. To further probe this, an additional S2 coating was deposited at a higher SOD. Increasing the SOD extended the residence time within the plasma plume, which significantly reduced the secondary phases, as shown in Fig. 6. This effect is attributed to the longer residence time allowing more complete decomposition and cation mixing prior to solidification on the substrate. S3, deposited at an intermediate enthalpy, produced a dense, well-adhered coating with a phase-pure rock-salt structure. These results highlight that a balanced window of process parameters including power, gas flow, SOD and gas mixture rather than enthalpy input alone, governs successful HEO phase formation and coating quality in SPPS.

The broader implication is that only a limited number of variables such as enthalpy input, stand-off distance, gas mixture and total gas flow were varied in this study, yet they already produced significant differences in coating microstructure and phase constitution, including the formation of a phase-pure HEO coating. However, the SPPS process is in fact governed by many more factors, including precursor feed rate, precursor concentration, injection geometry, plasma composition, and substrate temperature [20,22,36]. This means there are multiple pathways for appropriately manipulating spray conditions to achieve targeted outcomes in terms of phase purity, microstructure, and defect chemistry. While demonstrated here for a transition-metal rock-salt HEO, this thermodynamic-kinetic framework can be extended to other HEO families, including rare-earth systems for environmental barrier

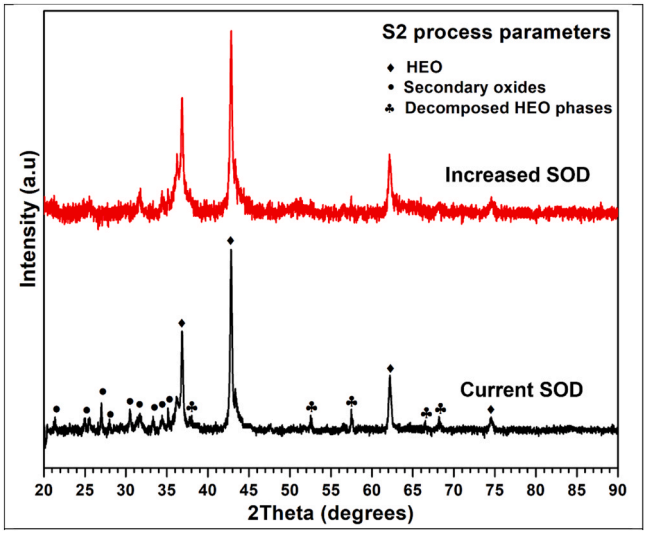

Fig. 6. XRD comparison of S2 coating deposited at the initial and increased stand-off distance, highlighting the reduction of secondary phases due to longer in-flight residence time.

coatings and spinel/perovskite systems for catalytic and functional roles. For energy-storage applications HEOs have attracted growing interest due to their electrochemical, catalytic, and high-temperature performance [37,38]. In particular, transition-metal HEOs such as (Co-Cu-Mg-Ni-Zn)O, (Fe-Co-Ni-Cu-Zn)O have already shown promising activity as anodes for lithium-ion batteries without lithium incorporation [6,39,40]. A logical next step would be to extend SPPS to Li-containing HEOs, which could reduce initial capacity losses and enhance Li-ion transport for LIBs, while also opening opportunities for all-solid-state batteries where Li-HEOs may serve as both active anodes and mixed ionic-electronic conductors.

5. Conclusion

This work demonstrates the single-step direct fabrication of (Co-Cu-Mg-Ni-Zn) high-entropy oxide coatings by solution precursor plasma spraying using an axial-feed capable torch. By incorporating both hydrate-bound and solvent water evaporation into the enthalpy balance, we show that the total energy requirement (~2.18 $kJ \cdot g^{-1}$ of solution) is well below the process enthalpies delivered by the plasma. Although only a limited set of process parameters was varied, the results reveal pronounced differences in coating microstructure and phase constitution, including the possibility of achieving a phase-pure HEO coating. This study underscores that, while SPPS provides sufficient thermal energy for single-phase formation, phase retention and coating adhesion are dictated by effective droplet-plasma interaction and residence time. Accordingly, a more comprehensive exploration of process parameters such as feed rate, SOD, injection geometry, gas flow distribution, and substrate thermal conditions will be essential to fully optimize HEO formation and coating quality. The thermodynamic-kinetic framework established here offers useful insights for adapting SPPS to varied HEO systems. This single-step, scalable route opens opportunities for deploying HEO coatings as functional electrodes in energy storage applications, while also providing a basis for extending the approach to high-temperature protective coatings such as TBCs and EBCs.

CRediT authorship contribution statement

Gidla Vinay: Writing – review & editing, Writing – original draft, Methodology, Investigation, Formal analysis. **Stefan Björklund:** Writing – review & editing, Investigation. **Ilari Angervo:** Writing – review & editing, Resources. **Ashish Ganvir:** Writing – review & editing, Supervision, Project administration, Methodology, Conceptualization. **Shrikant Joshi:** Writing – review & editing, Supervision, Project administration, Methodology, Conceptualization.

Declaration of Competing Interest

The authors declare that they have no known competing financial interests or personal relationships that could have appeared to influence the work reported in this paper.

Acknowledgement

The authors gratefully acknowledge Dr. Vasanth Gopal (University West) and Dr. Ermei Mäkilä (University of Turku) for assistance with sample preparation. Support from GREEN-BAT (Dnr 352517), co-funded by the Research Council of Finland, Vinnova (Swedish Governmental Agency for Innovation Systems) and the European Union under the M-ERA.NET 2021 framework, as well as the SOLACE (Dnr 360540) Academy research fellowship, funded by the Research Council of Finland enabled this work. Prof. Ashish Ganvir also extends his gratitude to the City of Turku for supporting his tenure-track grant and access to experimental facilities provided by the Finnish Digital Design and Manufacturing Infrastructure (FiDiEm).

Appendix A. Supporting information

Supplementary data associated with this article can be found in the online version at doi:10.1016/j.jeurceramsoc.2026.118150.

Data availability

Data will be made available on request.

References

[1] C.M. Rost, E. Sachet, T. Borman, A. Moballegh, E.C. Dickey, D. Hou, J.L. Jones, S. Curtarolo, J.-P. Maria, Entropy-stabilized oxides, Nat. Commun. 6 (2015) 8485.
[2] D. Bérardan, S. Franger, D. Dragoe, A.K. Meena, N. Dragoe, Colossal dielectric constant in high entropy oxides, Phys. Status Solidi RRL 10 (2016) 328–333.
[3] G. Du, C. Li, J. Li, G. Wu, Z. Huang, A. Mao, M. Ma, Z. Guo, Z. Chen, Research progress on high entropy oxide ceramics: principles, preparation, and properties, J. Mater. Res. Technol. 35 (2025) 265–288.
[4] B. Qian, Y. Wang, J. Zu, K. Xu, Q. Shang, Y. Bai, A review on multicomponent rare earth silicate environmental barrier coatings, J. Mater. Res. Technol. 29 (2024) 1231–1243.
[5] H. Vakilifard, H. Shahbazi, A.C. Liberati, R.B.N. Saraswathy, R.S. Lima, M.D. Pugh, C. Moreau, High entropy oxides as promising materials for thermal barrier topcoats: a review, J. Therm. Spray Tech. 33 (2024) 447–470.
[6] A. Sarkar, L. Velasco, D. Wang, Q. Wang, G. Talasila, L. de Biasi, C. Kübel, T. Brezesinski, S.S. Bhattacharya, H. Hahn, B. Breitung, High entropy oxides for reversible energy storage, Nat. Commun. 9 (2018) 3400.
[7] Y. Sun, S. Dai, High-entropy materials for catalysis: a new frontier, Sci. Adv. 7 (2021) eabg1600.
[8] P. Wei, S. Zhao, L. Zhuang, H. Yu, Y. Qin, Y. Chu, hemical co-precipitation synthesis of high-entropy rare-earth silicate nanopowders, J. Am. Ceram. Soc. 107 (2024) 3577–3586.
[9] A.J. Knorpp, A. Zawisza, S. Huangfu, A. Borzì, A.H. Clark, D. Kata, T. Graule, M. Stuer, Hydrothermal synthesis of multi-cationic high-entropy layered double hydroxides, RSC Adv. 12 (2022) 26362–26371.
[10] T. Mushiana, M. Khan, M.I. Abdullah, N. Zhang, M. Ma, Facile sol–gel preparation of high-entropy multielemental electrocatalysts for efficient oxidation of methanol and urea, Nano Res. 15 (2022) 5014–5023.
[11] S. Aydinyan, H. Kirakosyan, A. Sargsyan, O. Volobujeva, S. Kharatyan, Solution combustion synthesis of MnFeCoNiCu and $(MnFeCoNiCu)_3O_4$ high-entropy materials and sintering thereof, Ceram. Int. 48 (2022) 20294–20305.
[12] Y. Wang, J. Mi, Z.-S. Wu, Recent status and challenging perspective of high entropy oxides for chemical catalysis, Mater. Today Chem. 2 (2022) 1624–1656.
[13] S. Akrami, P. Edalati, M. Fuji, K. Edalati, High-entropy ceramics: review of principles, production and applications, Mater. Sci. Eng. R. Rep. 146 (2021) 100644.
[14] V. Gopal, K. Clovis, S. Björklund, A. Balapure, S. Goel, A. Hall, R. Younesi, S. Joshi, Exploring atmospheric plasma spraying as a pathway to fabricate solid-state battery constituents, Surf. Coat. Technol. 502 (2025) 131945.

[15] X. Liang, Y. Wang, X. Zhang, D. Han, L. Lan, Y. Zhang, Performance study of a $Li_4Ti_5O_{12}$ electrode for lithium batteries prepared by atmospheric plasma spraying, Ceram. Int. 45 (17B) (2019) 23750–23755.
[16] A. Hasani, S. Joshi, A. Salminen, S. Goel, J. Reuteler, M.G. Makowska, A. Ganvir, Localized phase and elemental mapping in solid-state lithium battery LTO anode thin-film produced by a novel suspension plasma spray approach, J. Therm. Spray. Technol. 34 (2025) 1589–1597.
[17] Y.-Q. Sun, X.-T. Luo, Y.-S. Zhu, X.-J. Liao, C.-J. Li, Li_3PO_4 electrolyte of high conductivity for all-solid-state lithium battery prepared by plasma spray, J. Eur. Ceram. Soc. 42 (10) (2022) 4239–4247.
[18] X. Liu, X. Li, Y. Li, H. Zhang, Q. Jia, S. Zhang, W. Lei, High-entropy oxide: a future anode contender for lithium-ion battery, EcoMat 4 (6) (2022) e12261.
[19] A. Pasupathi, M. Perumal, E. Narayanamoorthi, B. Palanisamy, Y. Subramaniam, Electrochemical charge storage performance of $(Mn, Ni, Mo, Co, Fe)_3O_4$ high entropy oxide nanoparticles produced via thermal plasma route, Ceram. Int. 50 (15) (2024) 26740–26749.
[20] A. Pasupathi, P. Kandasamy, R.K. Dharman, S. Govindarajan, T.H. Oh, M.W. Lee, Y. Subramaniam, A facile approach to deposit high performance electrocatalyst high entropy oxide coatings using a novel plasma spray route for efficient water splitting in an alkaline medium, Sustain, Energy Fuels 9 (2025) 3323–3334.
[21] Y. Lin, S. Chen, Y. Ma, S. Wang, Z. Ma, L. Sun, R. Cao, G. Song, Z. Yu, J. Yao, H. Liao, One-step, binder-free and rapid synthesis of high-entropy oxide anode materials for lithium-ion batteries, Next Mater 8 (2025) 100855.
[22] T. Hervy, N. Curry, S. Björklund, F. Lukac, S. Joshi, Axial plasma spraying of aqueous solution precursors: A facile approach for columnar thermal barrier coatings, J. Eur. Ceram. Soc. 45 (6) (2025).
[23] A. Sarkar, R. Djenadic, N.J. Usharani, K.P. Sanghvi, V.S.K. Chakravadhanula, A. S. Gandhi, H. Hahn, S.S. Bhattacharya, Nanocrystalline multicomponent entropy stabilised transition metal oxides, J. Eur. Ceram. Soc. 37 (2) (2017) 747–754.
[24] T.D. Desissa, M. Meja, D. Andoshe, F. Olu, F. Gochole, O.A. Zelekew, T. Temesgen, B. Brehane, K.D. Kuffi, T. Hunde, Synthesis and characterizations of (Mg, Co, Ni, Cu, Zn)O high-entropy oxides, SN, Appl. Sci. 3 (2021) 877.
[25] A.D. Dupuy, J.M. Schoenung, Morphological evolution in nanostructured secondary phases in entropy stabilized oxides, Mater. Charact. 193 (2022) 112301.
[26] J.E. Norman, A.D. Dupuy, J.M. Schoenung, Crystal lattice engineering of spinel phases in Mn-oxide doped (Co,Cu,Mg,Ni,Zn)O, Mater. Res. Lett. 13 (7) (2025) 729–738.
[27] X. Sun, Y. Xie, X. Meng, D. Mao, Z. Zhang, J. Wang, X. Ma, N. Wang, Y. Huang, Tailoring high-entropy oxides to ameliorate interfacial mismatch of aluminum-matrix composites towards superior strength–ductility balance, Mater. Sci. Eng. A 909 (2024) 146813.
[28] D. Bérardan, S. Franger, A.K. Meena, N. Dragoe, Room temperature lithium superionic conductivity in high entropy oxides, J. Mater. Chem. 4 (2016) 9536–9541.
[29] Y. Li, Y. Qiu, G. Yao, X. Mou, X. Liang, H. Huang, D. Huang, W. Zhou, S. Xu, J. Guo, Dual-phase (AlMgCoNiCuZn)O high-entropy oxide embedded in graphite nanosheets with superior lithium storage capability, J. Energy Storage 115 (2025) 115993.
[30] Z. Wang, X. Meng, Q. Guo, C. Su, G. Deng, H. Liu, Z. Yao, S. Zhang, H. Liu, H. Hao, Formation and evolution of oxygen vacancy layer in $BaTiO_3$ dielectric ceramics under thermal and electric field stimuli, Acta Mater. 299 (2025) 121450.
[31] H. Idriss, On the wrong assignment of the XPS O 1 s signal at 531–532 eV attributed to oxygen vacancies in photo- and electro-catalysts for water splitting and other materials applications, Surf. Sci. 712 (2021) 121894.
[32] G. Mauer, R. Vaßen, D. Stöver, Plasma and particle temperature measurements in thermal spray: approaches and applications, J. Therm. Spray. Technol. 20 (2011) 391–406.
[33] A.H. Phakatkar, M.T. Saray, M.G. Rasul, L.V. Sorokina, T.G. Ritter, T. Shokuhfar, R. Shahbazian-Yassar, Surface chemistry of multicationic transition metal oxides in electrochemical environments, Langmuir 37 (30) (2021) 9059–9068.
[34] K.H. Stern, High temperature properties and decomposition of inorganic salts Part 3. Nitrates and nitrites, J. Phys. Chem. Ref. Data 1 (3) (1972) 747–772.
[35] N.S. Osborne, H.F. Stimson, D.C. Ginnings, Measurements of heat capacity and heat of vaporization of water in the range of 0° to 100 °C, J. Res. Natl. Bur. Stand 23 (1939) 197–260.
[36] G. Mittal, S. Paul, Suspension and solution precursor plasma and HVOF spray: a review, J. Therm. Spray. Technol. 31 (2022) 1443–1475.
[37] X. Li, W. Zhang, K. Lv, J. Liu, A. Bayaguud, Research progress on high-entropy oxides as advanced anode, cathode, and solid-electrolyte materials for lithium-ion batteries, J. Power Sources 620 (2024) 235259.
[38] Y. Wu, M. Liu, A. Zhang, L. Ma, L. Ouyang, High-entropy oxides: a strategy for next-generation lithium and sodium-ion battery electrodes, Mater. Today 88 (2025) 1028–1042.
[39] H. Du, S. Wu, Y. Zhao, Non-equimolar high-entropy oxides with superior electrochemical performance: an example of (Mg-Co-Ni-Cu-Zn)O rock-salt oxides. J Mater Sci (2025).
[40] Y. Li, Z. Chen, J. Liu, R. Liu, C. Zhang, H. Li, Novel high entropy oxide as anode for high performance lithium-ion capacitors, Ceram. Int. 49 (23) (2023) 38439–38447.